Multifunctional Two-Dimensional $VSi_2N_4/WSi_2N_4/VSi_2N_4$ Photodetector Driven by the Photogalvanic Effect

Li Shu, Liyu Qian, Xiang Ye, and Yiqun Xie*
Department of Physics, Shanghai Normal University, Shanghai 200234, China

(Received 6 December 2021; revised 26 March 2022; accepted 12 April 2022; published 6 May 2022; corrected 19 May 2022)

Semiconducting monolayer $MoSi_2N_4$ and monolayer WSi_2N_4 have recently been fabricated and a number of two-dimensional (2D) materials with the same chemical formula and symmetry have been predicted, the mechanical, optical, and thermoelectric properties of which have been investigated. However, research regarding device applications of this 2D family have been very limited so far. Here, we propose a photodetector based on a 2D $VSi_2N_4/WSi_2N_4/VSi_2N_4$ lateral heterojunction, and investigate the transport properties of the photocurrent by using quantum transport simulations. The dependence of the photocurrent on the incident angle α and on the light-polarization angle θ is formulated. A robust photogalvanic effect is generated under the illumination of linearly polarized light due to the noncentrosymmetric C_{2v} symmetry of the photodetector. The photocurrent has a $\cos(2\theta)$ and $\cos(2\alpha)$ dependence on the light polarization and on the incident angle, respectively. A pure spin current, a perfect spin-filtering effect, and an excellent spin-valve effect can be achieved at zero bias for a broad photon energy range with an appropriate polarization angle at both normal and horizontal incidence. Moreover, at horizontal incidence, the photocurrent is highly polarization sensitive with an extinction ratio of up to 10^4. These results suggest that the 2D WSi_2N_4 family has promising multifunctional applications in low-power optoelectronics and spintronics.

DOI: 10.1103/PhysRevApplied.17.054010

I. INTRODUCTION

Recently, two-dimensional (2D) monolayers $MoSi_2N_4$ and monolayer WSi_2N_4 have been successfully fabricated by the chemical-vapor-deposition method, showing an excellent stability to air, water, acid, and heat [1]. Moreover, ten other 2D monolayers with the same chemical formula and symmetry (D_{3h}) have also been predicted, such as the magnetic monolayers VSi_2N_4 and $NbSi_2N_4$. This 2D family has attracted increasing research interest, which mainly focuses on its optical [2,3], magnetic [4], mechanical [5], and thermoelectrical properties [6–8], whereas the device applications have been rarely studied so far. Only a few recent theoretical studies have investigated the electrical transport properties of the 2D $MoSi_2N_4$ transistors by using quantum transport simulations [9,10]. Therefore, more efforts are needed to explore the potential device applications of this 2D family.

Among this 2D family, monolayer WSi_2N_4 is a nonmagnetic semiconductor with a band gap (2.076 eV) in the visible range, according to first-principles calculations using Heyd-Scuseria-Ernzerhof (HSE) functional [1], while monolayer VSi_2N_4 is predicted to be a half-metallic magnetic material with a Curie temperature above 300 K [4]. Monolayer WSi_2N_4 and monolayer VSi_2N_4 have similar lattice constants of 2.915 and 2.883 Å, respectively, with a small lattice mismatch about 1%. Moreover, first-principles study has predicted that monolayer WSi_2N_4 has an appropriate energy-band edge and high electron and hole mobility [1], as well as large visible-light absorption [11]. This therefore motivates us to consider a photodetector based on a $VSi_2N_4/WSi_2N_4/VSi_2N_4$ lateral heterojunction and to investigate the transport properties of the photocurrent under illumination by polarized light. We expect that a robust photogalvanic effect (PGE) will occur in the photodetector and that a spin-polarized photocurrent will be generated due to spin injection from the magnetic VSi_2N_4 electrodes. The PGE [12–16], which is also referred to as the bulk photovoltaic effect [17–24], occurs in materials without space-inversion symmetry and produces a direct photocurrent without the need for any external electrical fields (at zero bias) or p-n junctions. There has been an increased interest in the PGE in 2D materials due to its promising applications in various fields, including solar cells [25,26], photodetection [27–29], and spintronics [30–35]. In general, the PGE can be enhanced by reducing material symmetry [26,36–38]. For example, a recent experiment has shown that a vertical heterojunction composed of monolayer WSe_2 and phosphorene demonstrates a polarization-sensitive photocurrent due to the PGE. In this vertical heterojunction, the stacking of two different monolayers

*yqxie@shnu.edu.cn

breaks the space-inversion symmetry of monolayer phosphorene and also reduces the symmetry of monolayer WSe_2, leading to a robust PGE [39].

In this paper, we propose a multifunctional photodetector based on the monolayer $VSi_2N_4/WSi_2N_4/VSi_2N_4$ lateral heterojunction, where VSi_2N_4 serves as the metallic electrode and WSi_2N_4 is the semiconductor for photon harvesting. This photodetector has a reduced symmetry of C_{2v} with respect to the intrinsic D_{3h} symmetry of monolayers WSi_2N_4 and monolayer VSi_2N_4, which is beneficial for a robust PGE. Our quantum transport simulations show that the PGE is indeed generated in the photodetector when monolayer WSi_2N_4 is irradiated by linearly polarized light. The photocurrent is therefore produced at zero bias and a pure spin current and a perfect spin-filtering effect, as well as an outstanding spin-valve effect, can be generated for broadband photon energies with an appropriate polarization. Moreover, the photocurrent shows a high polarization sensitivity with an extinction ratio of up to 10^4. Therefore, the proposed photodetector has promising multifunctional applications in both low-power optoelectronics and spintronics.

II. MODEL AND METHODS

Figures 1(a) and 1(b) show top and side views of the atomic configuration of monolayer VSi_2N_4. The primitive cell has a lattice constant of $a = 2.883$ Å, as indicated by a red parallelogram in Fig. 1(a). Monolayer WSi_2N_4 has a similar configuration, except for a different lattice constant of 2.915 Å. To construct a $VSi_2N_4/WSi_2N_4/VSi_2N_4$ lateral heterojunction, we use the lattice constant of monolayer VSi_2N_4, which means a 1% contraction in the lattice of WSi_2N_4. Figures 1(c) and 1(d) show top and side views of the photodetector, respectively. The photodetector is divided into three parts, where the left and right electrodes are composed of monolayer VSi_2N_4 and in the center region WSi_2N_4 is sandwiched by monolayer VSi_2N_4. The photodetector is located in the x-z plane and a 27-Å vacuum layer is added in the y direction to remove interactions between periodical image cells. The two electrodes extend to $z = \pm\infty$, respectively, to mimic semi-infinite electrodes, while the whole device is periodical in the x direction. The monolayer WSi_2N_4 in the center region is irradiated by linearly polarized light, as indicated by the wavy arrows in Fig. 1(d). The magnetic moments of the two VSi_2N_4 electrodes can be in a parallel configuration (PC) or an antiparallel configuration (APC). The photocurrent flows along the z (armchair) direction from one electrode through the center region to another.

Optical absorption occurs in the monolayer WSi_2N_4 in the center region, which is irradiated by linearly polarized light. The electron-photon interaction can be described by the Hamiltonian $H' = \frac{e}{m_0}\mathbf{A}\cdot\mathbf{P}$, where e is the electron charge, m_0 is the electron mass, and $\mathbf{A}$ and $\mathbf{P}$ are the

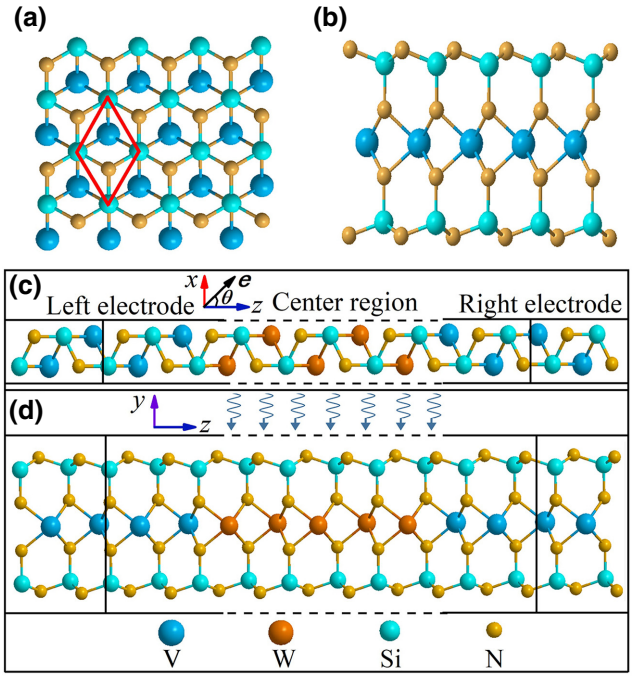

FIG. 1. (a),(b) Top and side views of monolayer VSi_2N_4: the primitive unit cell is indicated by a red parallelogram. (c),(d) Top and side views of a $VSi_2N_4/WSi_2N_4/VSi_2N_4$ photodetector, respectively. The wavy curves indicate linearly polarized light that shines on monolayer WSi_2N_4 in the center region. Vector $\mathbf{e}$ is the polarization vector, which forms an angle θ with respect to the z direction under normal incidence.

electromagnetic vector potential of light and the momentum of the electrons, respectively. The second-quantized vector potential $\mathbf{A}$ is given by [40]

$$\mathbf{A} = \mathbf{e}\left(\frac{\hbar\sqrt{\mu_r\varepsilon_r}}{2N\omega\varepsilon c}I_\omega\right)^{\frac{1}{2}}(be^{-i\omega t} + b^\dagger e^{i\omega t}), \qquad (1)$$

where ω is the photon frequency, N is the photon number, c is the light velocity, μ_r is the relative magnetic susceptibility, ε_r is the relative dielectric constant, I_ω is the photon flux, b and $b^\dagger$ are the bosonic annihilation and creation operators, and $\mathbf{e} = \cos\theta\mathbf{e}_1 + \sin\theta\mathbf{e}_2$ is the polarization vector of linearly polarized light, where θ is the angle formed by the polarization direction with respect to the vector $\mathbf{e}_1$. The incidence direction of the light is determined by the vector product $\mathbf{e}_1 \times \mathbf{e}_2$. Then, the second-quantized Hamiltonian can be written in matrix form as

$$H' = \sum_{l,m} M_{l,m}(\mathbf{P}_{l,m}\cdot\mathbf{e})(be^{-i\omega t} + b^\dagger e^{i\omega t})aa^\dagger, \qquad (2)$$

where l and m are atomic orbital labels, a and $a^\dagger$ are electron annihilation and creation operators, and $M_{l,m} = \frac{e}{m_0}\left(\frac{\hbar\sqrt{\mu_r\varepsilon_r}}{2N\omega\varepsilon c}I_\omega\right)^{\frac{1}{2}}$. Subsequently, the self-energy $\sum_{lm}^{>,<}(E)$

and then the greater or lesser Green's function $G^{>/<(\mathrm{ph})}(E)$ with electron-photon interactions can be calculated. Finally, the photocurrent flowing through a device can be obtained based on the linear response theory [40,41]. For details, we refer interested readers to Refs.[40] and [41]. Within the same methodology, we have deduced the photocurrent for linearly polarized light in the PGE in our previous work [42], in which the photocurrent injected into the lead L can be written as

$$\begin{aligned} J_L^{(\mathrm{ph})} = \frac{ie}{h}\int \{&\cos^2\theta \mathrm{Tr}\{\Gamma_L[G_1^{<(\mathrm{ph})} + f_L(G_1^{>(\mathrm{ph})} - G_1^{<(\mathrm{ph})})]\} \\ &+ \sin^2\theta \mathrm{Tr}\{\Gamma_L[G_2^{<(\mathrm{ph})} + f_L(G_2^{>(\mathrm{ph})} - G_2^{<(\mathrm{ph})})]\} \\ &+ 2\sin(2\theta)\mathrm{Tr}\{\Gamma_L[G_3^{<(\mathrm{ph})} \\ &+ f_L(G_3^{>(\mathrm{ph})} - G_3^{<(\mathrm{ph})})]\}\}dE, \end{aligned} \tag{3}$$

where the greater or lesser Green's functions ($G_{1,2,3}^{>/<(\mathrm{ph})}$) are determined by the material symmetry, the photon frequency, and the polarization vector **e**.

In this work, we consider both normal and oblique incidence of linearly polarized light. For normal incidence, polarized light shines vertically on monolayer WSi_2N_4 in the center region along the y axis and the polarization plane is in the x-z plane. In this case, the polarization vector **e** forms a polarization angle θ with respect to the z direction, as indicated in Fig. 1(c). For oblique incidence, assuming that the incidence plane is in the x-y plane, we can set $\mathbf{e}_2$ along the z direction, i.e., $\mathbf{e}_2 = e_{2z}\mathbf{k} = 1\mathbf{k}$, and $\mathbf{e}_1 = \cos\alpha\mathbf{i} + \sin\alpha\mathbf{j}$, where **i**, **j**, and **k** are the unit vectors of the x, y, and z axes, respectively. Here, the incidence angle α is formed by the transport direction of light with respect to the y axis. Consequently, we can rewrite Eq. (3) as

$$J_L^{(\mathrm{ph})} = \frac{ie}{h}\int \mathrm{Tr}\{\Gamma_L[G_4^{<(\mathrm{ph})} + f_L(G_4^{>(\mathrm{ph})} - G_4^{<(\mathrm{ph})})]dE, \tag{4}$$

where

$$\begin{aligned} G_4^{>/<(\mathrm{ph})} = {}& C_0\cos^2\alpha\cos^2\theta\left(G_0^r p_x^\dagger G_0^{>/<} p_x G_0^a\right) + C_0\sin^2\alpha\cos^2\theta\left(G_0^r p_y^\dagger G_0^{>/<} p_y G_0^a\right) \\ &+ \frac{C_0}{2}\cos\alpha\sin(2\theta)\left(G_0^r p_z^\dagger G_0^{>/<} p_x G_0^a + G_0^r p_x^\dagger G_0^{>/<} p_z G_0^a\right) \\ &+ \frac{C_0}{2}\sin\alpha\sin(2\theta)\left(G_0^r p_z^\dagger G_0^{>/<} p_y G_0^a + G_0^r p_y^\dagger G_0^{>/<} p_z G_0^a\right) \\ &+ C_0\sin(2\alpha)\cos^2\theta\left(G_0^r p_y^\dagger G_0^{>/<} p_x G_0^a + G_0^r p_x^\dagger G_0^{>/<} p_y G_0^a\right) \\ &+ C_0\sin^2\theta\left(G_0^r p_z G_0^{>/<} p_z^\dagger G_0^a\right). \end{aligned} \tag{5}$$

Equation (5) describes the dependence of the PGE photocurrent on both the incidence angle α and the polarization angle θ, which is determined by material symmetry. Here, $C_0 = (e/m_0)^2\frac{\hbar\sqrt{\mu_r\epsilon_r}}{2\omega\epsilon c}I_\omega$, $G_0^{r/a}$ are the retarded or advanced Green's functions without photons and $G_0^{>/<}$ are the greater or lesser Green's functions without photons. The photocurrent can be normalized as $I = J_L^{(\mathrm{ph})}/eI_\omega$, which still has a dimension of the area, i.e., a_0^2 per photon, where a_0 is the Bohr radius.

The above method to calculate the PGE photocurrent is implemented in the quantum transport package NANODCAL [43,44] and in the following all the calculations are performed using NANODCAL. The photocurrent is calculated using the following procedure. First, we calculate the Hamiltonian (H_0) of the device by using first-principles methods, i.e., density-functional theory (DFT) carried out within the Keldysh nonequilibrium Green's function (NEGF) formalism [43]. Second, the Hamiltonian of the electron-photon interaction (H') is calculated and subsequently the self-energy $\sum_{lm}^{>,<}(E)$ and $G_{1,2,3}^{>/<(\mathrm{ph})}$ is calculated based on the total Hamiltonian ($H_0 + H'$). Finally, the photocurrent is obtained by using Eqs. (3)–(5). In the electronic self-consistent calculations for the electrodes and the center region, the Brillouin zone is sampled using $10 \times 1 \times 150$ and $10 \times 1 \times 1$ grids of k points, respectively. In the photocurrent-transport calculation, $20 \times 1 \times 1$ k points are used. The double-zeta-polarized atomic orbital basis is used to expand all the physical quantities, the exchange and correlation are treated at the level of the generalized-gradient-approximation functional as parametrized by Perdew, Burke, and Ernzerhof [45], and the atomic cores are defined by the standard norm-conserving nonlocal pseudopotentials.

III. RESULTS AND DISCUSSION

We consider the photocurrent for linearly polarized light with photon energies in the visible range from 1.6 to 3.2 eV and calculate the photocurrent at intervals of 0.1 eV. Simulations show that at both normal and oblique incidence, the PGE is induced and a robust photocurrent is produced in the $VSi_2N_4/WSi_2N_4/VSi_2N_4$ photodetector due to the noncentrosymmetric C_{2v} symmetry.

The magnetic VSi_2N_4 electrodes enable spin injection into WSi_2N_4 in the central region and hence the photocurrent is spin polarized. In order to discuss the spin-dependent transport properties of the photocurrent, we define the spin-injection efficiency as $\eta_s \equiv \big||I_\uparrow| - |I_\downarrow|/|I_\uparrow| + |I_\downarrow|\big| \times 100\%$, where $I_\uparrow$ and $I_\downarrow$ denote the spin-polarized photocurrent contributed by spin-up and spin-down channels, respectively. η_s measures the degree of spin polarization of the transport current in the device. Once $I_\uparrow$ or $I_\downarrow$ disappear, $\eta_s = 100\%$, resulting in a fully spin-polarized photocurrent (FSPC), which means a perfect spin-filtering effect. The magnetoresistance ratio is defined as $\eta_m \equiv ||I_{PC}| - |I_{APC}|/|I_{PC}| + |I_{APC}||$, where I_{PC} and I_{APC} are the photocurrents for situations where the magnetic moments of the two electrodes are in the PC and the APC, respectively. According to the above definition, the maximum value of η_m is 1 when either I_{PC} or I_{APC} vanishes, indicating a perfect spin-valve effect. The total photocurrent $I = I_\uparrow + I_\downarrow$ and the spin current (I_s) is conventionally defined as $I_s = I_\uparrow - I_\downarrow$. If $I_\uparrow = -I_\downarrow$, that is, the two spin currents have the same magnitude with opposite directions, the total charge current vanishes ($I = 0$). However, the spin current $I_s \neq 0$, which means that a pure spin current (PSC) is generated.

A. The PGE under normal incidence of linearly polarized light

We find that, under normal incidence ($\alpha = 0$), the photocurrent shows a cosine dependence on the polarization angle θ in both the PC and the APC, with a form $I = I_0 + A\cos(2\theta)$. As examples, Fig. 2(a) gives the photocurrent as a function of θ for photon energies of 1.9, 2.0, and 2.1 eV in the PC. It can be seen that the photocurrent of 1.9 eV (black circles) is fitted very well with a function $I = 0.2 + 0.1\cos(2\theta)$ (the solid brown line). Figure 2(b) shows the total photocurrent and the spin-up and spin-down photocurrents at 3.1 eV in the APC, respectively. The total current (blue circles) is also well fitted with a function $I = 2.2 + 1.5\cos(2\theta)$ (the solid brown line). The maximum photocurrent therefore occurs at the polarization angle $\theta = 0^\circ$ or 90° due to this $\cos(2\theta)$ dependence. We then give, in Fig. 2(c), the maximum photocurrent ($I_{\max}$) for different photon energies in the PC and APC. This shows that $I_{\max}$ for the APC is evidently larger than that for the PC in a higher photon energy range from 2.6 to 3.2 eV, with a maximum of 5.3 at 3.0 eV. As the photocurrent is

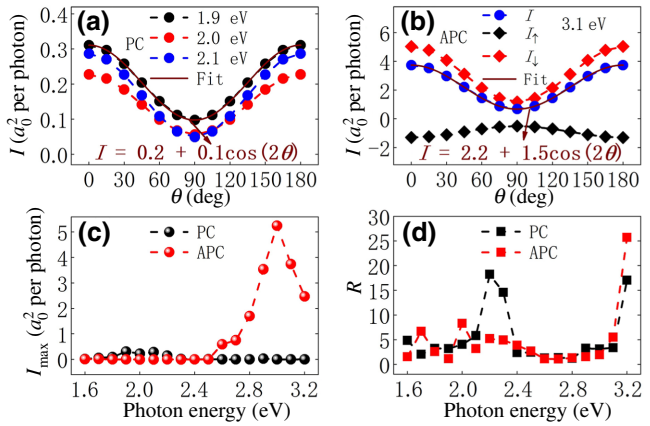

FIG. 2. (a) The variation of the photocurrent with the polarization angle θ for photon energies of 1.9, 2.0, and 2.1 eV in the PC and (b) the total photocurrent and the spin-up and spin-down photocurrents at 3.1 eV in the APC. (c) The maximum photocurrent and (d) the extinction ratio at different photon energies for the PC and APC, respectively.

polarization dependent, we define the extinction ratio R as the ratio of the maximum photocurrent to the minimum to evaluate the polarization sensitivity. The extinction ratios for the PC and APC are shown in Fig. 2(d) for different photon energies. It can be seen that R is greater than 5 for several photon energies and the maximum R is 25.7 at 3.2 eV for the APC, while is 18 at 2.2 eV for the PC.

Next, we study the spin-transport properties of the photocurrent. We find that either $I_\uparrow$ or $I_\downarrow$ vanishes at a certain polarization angle θ for some photon energies, which means that a FSPC is generated ($\eta_s = 100\%$). For example, $I_\downarrow = 0$ at $\theta = 70^\circ$ for 3.2 eV in the PC, as shown in Fig. 3(a). We find that there are six photon energies for which a FSPC can be generated in the PC, while the FSPC does not appear in the APC. Figure 3(b) gives the photon energies and the corresponding θ at which the FSPC is generated for the PC.

Furthermore, we calculate η_m at the different polarization angles θ for different photon energies. We find that at certain polarization angles, either I_{APC} or I_{PC} vanishes, producing a perfect spin-valve effect with $\eta_m = 1$. For instance, I_{APC} is zero at $\theta = 20^\circ$ for 1.7 eV, as shown in Fig. 3(c). Figure 3(d) shows the photocurrent (the black circles) and θ (the blue stars) at which $\eta_m = 1$. It can be seen that, among the ten photon energies where $\eta_m = 1$, the largest photocurrent is 4.8 for 3.0 eV at $\theta = 22^\circ$. Moreover, the PSC can be generated in both the PC and APC for some photon energies. For example, Fig. 3(e) shows that the total current (the blue circles) is zero at $\theta = 82^\circ$ for 3.2 eV in the APC and, meanwhile, $I_\uparrow$ and $I_\downarrow$ are equal in magnitude and opposite in direction, which leads to a PSC. In Fig. 3(f), we present all the photon energies and the corresponding polarization angles at which the PSC is generated for both the PC and APC. It can be seen that the

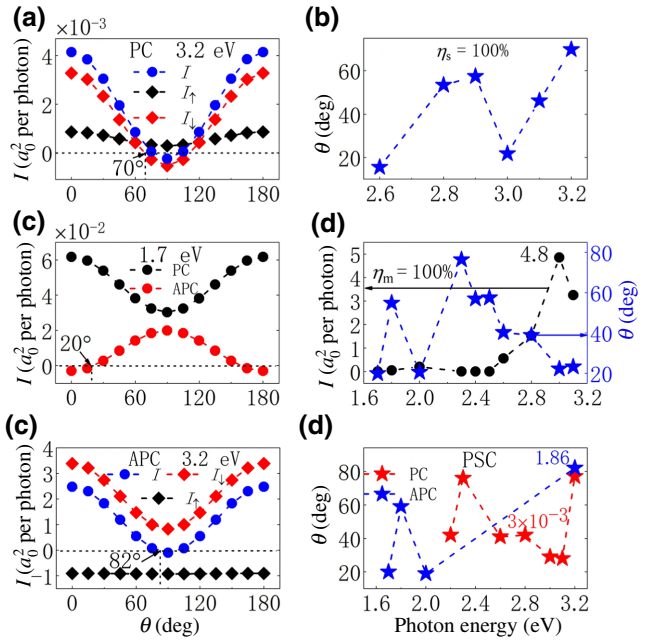

FIG. 3. (a) Under normal incidence, the total photocurrent and spin-polarized photocurrent for 3.2 eV in the PC, where a FSPC is produced at $\theta = 70°$. (b) The polarization angle θ at which a FSPC is produced in the PC. (c) The total photocurrent at 1.7 eV in the PC and APC, respectively. (d) The photocurrent (black) and polarization angle (blue) for $\eta_m = 1$. (e) The total photocurrent I and the spin-polarized photocurrents at 3.2 eV in the APC, where a PSC is generated at $\theta = 82°$. (f) The polarization angle and photon energies at which a PSC can be generated in the PC and APC, respectively.

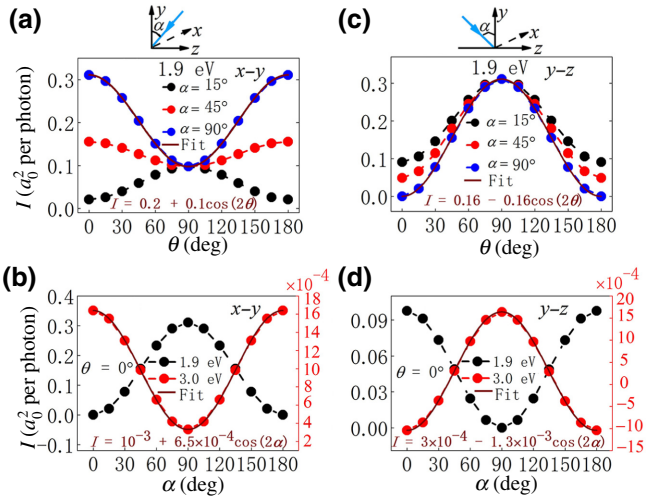

FIG. 4. Under oblique incidence, the variation of the photocurrent with the polarization angle θ at $\alpha = 15°$, 45°, and 90° for a photon energy of 1.9 eV within the (a) x-y and (c) y-z incidence planes, respectively. (b),(d) The corresponding variation of the photocurrent with α at $\theta = 0°$ for photon energies of 1.9 and 3.0 eV, respectively.

maximum PSC in the PC is 3×10^{-3} at $\theta = 42°$ for 2.8 eV and in the APC is 1.86 at $\theta = 82°$ for 3.2 eV.

B. The PGE under oblique incidence of linearly polarized light

For oblique incidence, we consider two incidence planes, namely, the x-y and y-z planes, respectively. Calculations show that under oblique incidence with different incidence angles α, the photocurrent still has a cosine dependence on the polarization angle θ. Figure 4(a) shows the variation of the photocurrent with θ at $\alpha = 15°$, 45°, and 90°, respectively, for a photon energy of 1.9 eV within the x-y incidence plane. We observe that at the same θ, the photocurrent increases with the increase of α. Figure 4(b) plots the photocurrent as a function of α at $\theta = 0°$ for photon energies of 1.9 and 3.0 eV, which can be perfectly fitted by the function $I = I_0 + B\ \cos(2\alpha)$. For oblique incidence within the y-z plane, the behavior of the photocurrent is similar to that within the x-y incidence plane. The photocurrent still has a $\cos(2\theta)$ dependence, as shown in Fig. 4(c). Besides, the photocurrent also has a form $I = I_0 + B\ \cos(2\alpha)$ at a given θ, as shown in Fig. 4(d).

According to the above analysis, the maximum photocurrent ($I_{\max}$) appears at either $\alpha = 0$ or 90°, which corresponds to incidence directions along the x, z, and y axes, respectively. Therefore, we give the maximum photocurrent for the light propagating along these three directions, as shown in Fig. 5(a). It can be seen that $I_{\max}$ along the x axis (the red spheres) is smaller than that along the y and z axes. For photon energies below 2.6 eV, $I_{\max}$ is almost the same for incidence along the y and z axes, while above 2.6 eV, $I_{\max}$ along the z axis (the blue spheres) is evidently larger than that (the black spheres) along the y axis. Figure 6(b) shows the corresponding extinction ratio for these three incidence directions. It can be seen that the extinction ratio for horizontal incidence along the x and z axes can be as high as 10^4 for photon energies from 1.6 to 2.0 eV. In particular, the largest extinction ratio is 6.89×10^4 at 1.6 eV along the z axis, which is much greater than that of normal (y-axis) incidence (25.7). This indicates that horizontal incidence can greatly enhance the polarization sensitivity of the photodetector. Finally, we discuss the spin-transport properties of the photocurrent under horizontal incidence. It can be seen from Fig. 5(c) that a FSPC can be generated for a number of photon energies. Moreover, Fig. 5(d) shows that a PSC can be produced for incidence along the x axis. Compared with normal incidence, x-axis incidence can produce the FSPC and PSC in a wider photon energy range, along with a much higher polarization sensitivity.

We now obtain that, first, the photocurrent for both normal and oblique incidence is proportional to $\cos(2\theta)$ and at a given θ the photocurrent shows a $\cos(2\alpha)$ dependence on

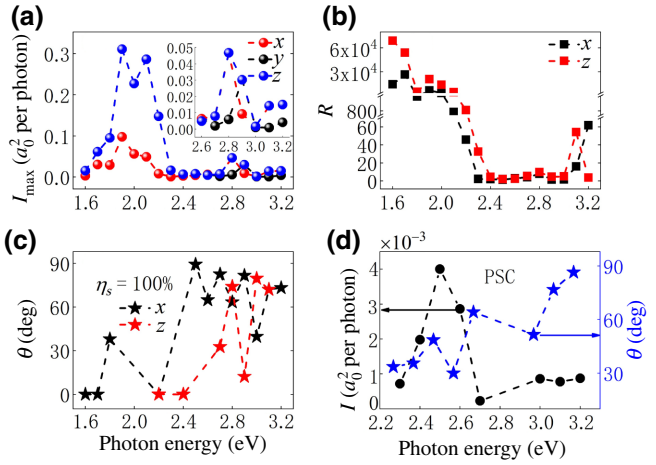

FIG. 5. (a) The maximum photocurrent generated under horizontal incidence along the x and z axes and under normal incidence along the y axis. (b) The corresponding extinction ratio. (c) The polarization angles at which a FSPC is generated under horizontal incidence along the x and z axes. (d) The PSC (black circles) generated at horizontal incidence along the x axis and the corresponding polarization angle θ (blue stars).

the incidence angle α. This behavior comes from the first two terms in Eq. (5) and is allowed by the C_{2v} symmetry for linearly polarized light, while the other three terms in Eq. (5) are forbidden by this symmetry. The dependence of the PGE photocurrent on the incidence direction has been experimentally investigated in GaAs/(Al,Ga)As quantum wells with C_s symmetry for circularly polarized light [46,47] and in several 2D materials with C_{2v} [48–51] and C_{3v} symmetry [52] for circularly polarized light,

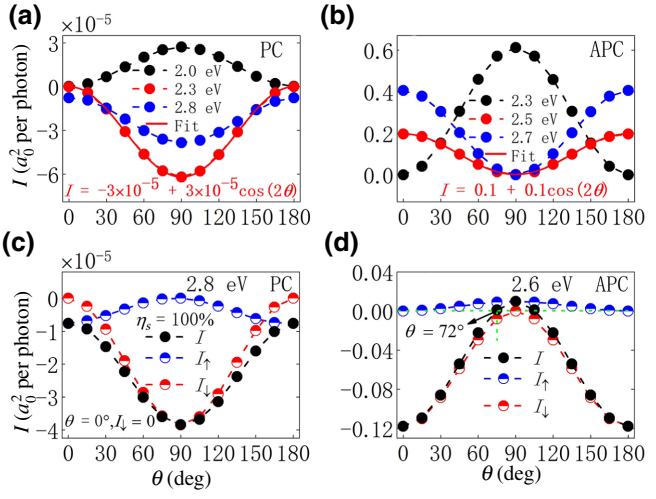

FIG. 6. (a) The photocurrent generated along the zigzag direction under normal incidence in the PC and (b) APC, respectively. (c) The photocurrent of 2.8 eV in the PC, where $\eta_s = 100\%$ is achieved at $\theta = 0°$. (d) The photocurrent of 2.6 eV, which has a PSC of 0.018 at $\theta = 72°$.

in which $\cos(\alpha)$ and $\sin(\alpha)$ dependence on the incidence angle have been observed, respectively. Second, the proposed 2D $VSi_2N_4/WSi_2N_4/VSi_2N_4$ photodetector shows a remarkably high polarization sensitivity. In our previous work [53], we have proposed polarization-sensitive photodetectors based on several 2D wide-band-gap materials of C_{3v} symmetry, with the largest extinction ratio being up to 280. Interestingly, in recent experiments, PGE-driven photodetectors have been realized by using 2D perovskite ferroelectric materials [27,28], which have demonstrated a good polarization sensitivity of 15. Besides, a number of photodetectors based on 2D materials have shown a polarization sensitivity [54–62]. So far, the largest extinction ratio measured in experiments is 111.2, which has been achieved by using a 2D graphene/$PdSe_2$/Ge photodetector [63]. Third, our proposed photodetector is able to generate both the FSPC and PSC in a broad photon energy range for both normal and horizontal incidence. The generation of the PSC by the PGE in a noncentrosymmetric system has been proposed previously by us [35] and has recently been proposed in a centrosymmetric 2D system [33]. Finally, the PGE proposed in this work could be generalized to photodetectors based on the same 2D family, such as monolayer $MoSi_2N_4$ and $NbSi_2N_4$, etc.

We also calculate the photocurrent along the zigzag direction and find that it also has a $\cos(2\theta)$ dependence on the polarization angle and, moreover, that the FSPC and PSC can also be obtained at some photon energies. Figures 6(a) and 6(b) show the photocurrent for some photon energies as a function of the polarization angle in a form of $\cos(2\theta)$ in the PC and APC, respectively. Figure 6(c) is the photocurrent of 2.8 eV in the PC, where $\eta_s = 100\%$ is achieved at $\theta = 0°$, and (d) is the photocurrent of 2.6 eV, which has a PSC of 0.018 at $\theta = 72°$. Therefore, both the FSPC and PSC can also be achieved in the zigzag direction for some photon energies at an appropriate polarization angle.

C. Discussion

It is worth noting that at oblique incidence, other mechanisms such as the photon-drag effect (PDE) may occur and may contribute to the photocurrent. The PDE can generate an in-plane photocurrent at oblique incidence, which is not restricted by an inversion symmetry, as the PDE coefficient is mathematically a fourth-rank tensor [64]. The photocurrent generated in the PDE is caused by the (angular and/or translational) momentum transfer from photons to electrons [65–67]. However, the momentum of photons is neglected in theory of the PGE and is not included in the Hamiltonian of the system. Instead, it is the electromagnetic vector potential $\mathbf{A}$ that contributes to the photon-electron interaction, the Hamiltonian of which is described by a form $e(\mathbf{A}\cdot\mathbf{P})/m_0$ (see Sec. II). This form of the photon-electron interaction is also generally accepted

in theories for the calculation of the bulk photovoltaic effect [20,21,68]. Therefore, the physics of the PDE is not included within our method for calculating the photocurrent. Nevertheless, the PDE of our system deserves future study with an appropriate method, which can be compared with the PGE.

Moreover, there is a difference between the PGE in a device and that in bulk materials. In our device model, the semiconducting WSi_2N_4 in the center region is irradiated by linearly polarized light, which induces photoexcited electrons that flow out of the center region by tunneling through the VSi_2N_4/WSi_2N_4 interface into the left and right electrodes with different probability, leading to a net PGE photocurrent at a zero bias. The physical mechanisms for the generation of the PGE photocurrent in semiconductor (WSi_2N_4) in the center region are similar to those in bulk materials. However, the electronic structures (e.g., the band structure, the Fermi level, etc.) of the semiconductor in the center region are inevitably influenced by the electrodes. For example, a recent experiment has shown that metal-$MoSe_2$ contact reduces the D_{3h} symmetry of monolayer $MoSe_2$ and thereby enables the generation of a PGE photocurrent even under the normal incidence of circularly polarized light, which is otherwise forbidden under D_{3h} symmetry [69]. Therefore, electrodes can change the symmetry of a bulk material and, moreover, the metal-semiconductor contact usually leads to band bending and hence a Schottky barrier for electron tunneling. All these aspects will change the photocurrent originally generated in bulk materials. This means that the PGE photocurrent in a device is different from that in bulk materials, as electrodes play an important role in determining the photocurrent. The importance of electrodes for the PGE photocurrent has also been investigated in several experiments [70,71].

Besides, in our device there is a VSi_2N_4/WSi_2N_4 interface located in the center region. For this metal-semiconductor interface, Fermi-level pinning (FP) may be induced and hence may influence the photocurrent. It is generally accepted that some aspects contribute to the FP in 2D metal-semiconductor junctions [72], such as metal-induced gap states (MIGS) formed in the semiconductor, which can be occupied by electrons and holes and therefore pin the Fermi level, and defects at the interface, which can generate gap states that pin the Fermi level, as well as the interface dipole formed by charge redistribution at the interface, which can change the original electronic levels. In our model, there are no defects in the interface, while defects can be created in real experiments. Here, we mainly check the MIGS that can possibly be induced in the VSi_2N_4/WSi_2N_4 interface. Based on our first-principles calculations of the center region, we obtain the local density of states (LDOS) in the center region when the magnetic moments of two electrodes are in the PC configuration and we plot the LDOS for spin-down

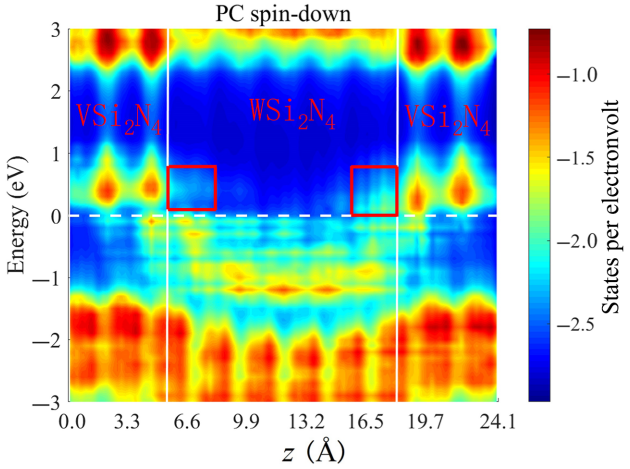

FIG. 7. The logarithmic LDOS of spin-down electrons in the center region of the $VSi_2N_4/WSi_2N_4/VSi_2N_4$ photodetector for the PC. The white solid line indicates the VSi_2N_4/WSi_2N_4 interface. The MIGS are indicated by two red rectangles. The Fermi level is set at 0 eV, indicated by the white dashed line.

electrons along the transport (z) direction, as shown in Fig. 7. The VSi_2N_4/WSi_2N_4 interface is indicated by white solid lines. The Fermi energy level is set at 0 eV, indicated by a white dotted line. We observe that WSi_2N_4 in the center region has an evident energy gap of about 2.3 eV, while the monolayer VSi_2N_4 shows a metallic property, as it has an abundant LDOS across the Fermi level. These electronic properties are in good agreement with previous first-principles calculations [1]. Notably, we find that there are evident LDOS across the Fermi level in WSi_2N_4 at the interface, as indicated by the red rectangles. These are MIGS induced by metallic VSi_2N_4 electrodes and they may lead to the FP. Therefore, the effect of the FP is naturally involved within the Hamiltonian of the center region and hence the influence of the FP on the PGE photocurrent is also included in our simulations.

We note that there are limitations in our photocurrent calculations by using the NEGF method within a ballistic transport regime. This method does not consider the kinetic process of the electron scattering possibly caused by phonons during their transport process, which leads to both momentum and energy relaxations. Ballistic transport can take place in our proposed photodetector at a low enough temperature with a finite channel length that is shorter than the free mean path of the electrons and therefore phonon scattering can be severely suppressed.

IV. CONCLUSIONS

In summary, we study the PGE in the 2D $VSi_2N_4/WSi_2N_4/VSi_2N_4$ photodetector at both normal and oblique incidence of linearly polarized light by using quantum transport simulations. The photocurrent has a cosine

dependence on the polarization angle θ and on the incidence angle α, which is determined by the C_{2v} symmetry of the photodetector. Under both normal and horizontal incidence, a perfect spin-filtering effect and spin-valve effect can be generated for a number of photon energies with an appropriate polarization angle. In particular, the FSC and PSC can be generated in a wider photon energy range for horizontal incidence along the x axis and, moreover, a much higher polarization sensitivity up to 10^4 can be obtained, as compared to normal incidence along the y axis. These results shed light on potential device applications of the 2D VSi_2N_4 family in low-power spintronics and optoelectronics.

ACKNOWLEDGMENTS

This work is supported by the National Natural Science Foundation of China under Grant No. 51871156.

[1] Y. L. Hong, Z. B. Liu, L. Wang, T. Y. Zhou, W. Ma, C. Xu, S. Feng, L. Chen, M. L. Chen, D. M. Sun, X. Q. Chen, H. M. Cheng, and W. C. Ren, Chemical vapor deposition of layered two-dimensional $MoSi_2N_4$ materials, Science **369**, 670 (2020).

[2] Y. D. Yu, J. Zhou, Z. L. Guo, and Z. M. Sun, Novel two-dimensional Janus $MoSiGeN_4$ and $WSiGeN_4$ as highly efficient photocatalysts for spontaneous overall water splitting, ACS Appl. Mater. Inter. **13**, 28090 (2021).

[3] J. F. Zhao, Y. L. Zhao, H. J. He, P. W. Zhou, Y. Liang, and T. Frauenheim, Stacking engineering: A boosting strategy for 2D photocatalysts, J. Phys. Chem. Lett. **12**, 10190 (2021).

[4] M. R. K. Akanda and R. K. Lake, Magnetic properties of $NbSi_2N_4$, VSi_2N_4, and VSi_2P_4 monolayers, Appl. Phys. Lett. **119**, 052402 (2021).

[5] A. Bafekry, M. Faraji, D. M. Hoat, M. Shahrokhi, M. M. Fadlallah, F. Shojaei, S. A. H. Feghhi, M. Ghergherehchi, and D. Gogova, $MoSi_2N_4$ single-layer: A novel two-dimensional material with outstanding mechanical, thermal, electronic and optical properties, J. Phys. D: Appl. Phys. **54**, 155303 (2021).

[6] Y. Yin, M. Yi, and W. L. Guo, High and anomalous thermal conductivity in monolayer MSi_2N_4 semiconductors, ACS Appl. Mater. Inter. **13**, 45907 (2021).

[7] B. Mortazavi, F. Shojaeic, B. Javvajia, T. Rabczuk, and X. Y. Zhuang, Outstandingly high thermal conductivity, elastic modulus, carrier mobility and piezoelectricity in two-dimensional semiconducting CrC_2N_4: A first-principles study, Mater. Today Energy **22**, 100839 (2021).

[8] J. H. Yu, J. Zhou, X. G. Wan, and Q. F. Li, High intrinsic lattice thermal conductivity in monolayer $MoSi_2N_4$, New J. Phys. **23**, 033005 (2021).

[9] J. S. Huang, P. Li, X. X. Ren, and Z. X. Guo, Promising Properties of a Sub-5-nm Monolayer $MoSi_2N_4$ Transistor, Phys. Rev. Appl. **16**, 044022 (2021).

[10] X. T. Sun, Z. G. Song, N. N. Huo, S. Q. Liu, C. Yang, J. Yang, W. Z. Wang, and J. Lu, Performance limit of monolayer $MoSi_2N_4$ transistors, J. Mater. Chem. C **9**, 14683 (2021).

[11] B. Mortazavi, B. Javvaji, F. Shojaei, T. Rabczuk, A. V. Shapeev, and X. Y. Zhuang, Exceptional piezoelectricity, high thermal conductivity and stiffness and promising photocatalysis in two-dimensional $MoSi_2N_4$ family confirmed by first-principles, Nano Energy **82**, 105716 (2021).

[12] V. I. Belinicher and B. I. Sturman, The photogalvanic effect in media lacking a center of symmetry, Sov. Phys. Usp. **23**, 199 (1980).

[13] S. Hubmann, G. V. Budkin, M. Otteneder, D. But, D. Sacré, I. Yahniuk, K. Diendorfer, V. V. Bel'kov, D. A. Kozlov, N. N. Mikhailov, S. A. Dvoretsky, V. S. Varavin, V. G. Remesnik, S. A. Tarasenko, W. Knap, and S. D. Ganichev, Symmetry breaking and circular photogalvanic effect in epitaxial $Cd_xHg_{1-x}Te$ films, Phys. Rev. Mater. **4**, 043607 (2020).

[14] M. M. R. Moayed, F. Li, P. Beck, J. C. Schobera, and C. Klinke, Anisotropic circular photogalvanic effect in colloidal tin sulfide nanosheets, Nanoscale **12**, 6256 (2020).

[15] O. Neufeld, N. T. Dejean, U. D. Giovannini, H. Hübener, and A. Rubio, Light-Driven Extremely Nonlinear Bulk Photogalvanic Currents, Phys. Rev. Lett. **127**, 126601 (2021).

[16] D. Rees, B. Z. Lu, Y. Sun, K. Manna, R. Özgür, S. J. Subedi, H. Borrmann, C. Felser, J. Orenstein, and D. H. Torchinsky, Direct Measurement of Helicoid Surface States in RhSi Using Nonlinear Optics, Phys. Rev. Lett. **127**, 157405 (2021).

[17] V. I. Belinicher, E. L. Ivchenko, and B. I. Sturman, Kinetic theory of the displacement photovoltaic effect in piezoelectrics, Sov. Phys. **56**, 359 (1982).

[18] V. I. Belinicher and B. I. Sturman, The relation between shift and ballistic currents in the theory of photogalvanic effect, Ferroelectrics **83**, 29 (1988).

[19] B. I. Sturman, Ballistic and shift currents in the bulk photovoltaic effect theory, Phys.-Usp. **63**, 407 (2020).

[20] W. Kraut and R. von Baltz, Anomalous bulk photovoltaic effect in ferroelectrics: A quadratic response theory, Phys. Rev. B **19**, 1548 (1979).

[21] R. von Baltz and W. Kraut, Theory of the bulk photovoltaic effect in pure crystals, Phys. Rev. B **23**, 5590 (1981).

[22] J. E. Sipe and A. I. Shkrebtii, Second-order optical response in semiconductors, Phys. Rev. B **61**, 5337 (2000).

[23] L. Z. Tan, F. Zheng, S. M. Y oung, F. Wang, S. Liu, and A. M. Rappe, Shift current bulk photovoltaic effect in polar materials—hybrid and oxide perovskites and beyond, npj Comput. Mater. **2**, 16026 (2016).

[24] A. M. Cook, B. M. Fregoso, F. de Juan, S. Coh, and J. E. Moore, Design principles for shift current photovoltaics, Nat. Commun. **8**, 14176 (2017).

[25] M. M. Yang, D. J. Kim, and M. Alexe, Flexo-photovoltaic effect, Science **360**, 904 (2018).

[26] Y. J. Zhang, T. Ideue, M. Onga, F. Qin, R. Suzuki, A. Zak, R. Tenne, J. H. Smet, and Y. Iwasa, Enhanced intrinsic photovoltaic effect in tungsten disulfide nanotubes, Nature **570**, 349 (2019).

[27] C. M. Ji, D. Dey, Y. Peng, X. T. Liu, L. N. Li, and J. H. Luo, Ferroelectricity-driven self-powered ultraviolet photodetection with strong polarization sensitivity in a two-dimensional halide hybrid perovskite, Angew. Chem. Int. Ed. **59**, 18933 (2020).

[28] Y. Peng, X. T. Liu, Z. H. Sun, C. M. Ji, L. N. Li, Z. Y. Wu, S. S. Wang, Y. P. Yao, M. C. Hong, and J. H. Luo, Exploiting the bulk photovoltaic effect in a 2D trilayered hybrid ferroelectric for highly sensitive polarized light detection, Angew. Chem. Int. Ed. **59**, 3933 (2020).

[29] S. S. Li, T. Wang, X. S. Chen, W. Lu, Y. Q. Xie, and Y. B. Hu, Self-powered photogalvanic phosphorene photodetectors with high polarization sensitivity and suppressed dark current, Nanoscale **10**, 7694 (2018).

[30] P. Jiang, X. X. Tao, H. Hao, Y. S. Liu, X. H. Zheng, and Z. Zeng, Two-dimensional centrosymmetrical antiferromagnets for spin photogalvanic devices, npj Quantum Inform. **21**, 7 (2021).

[31] S. M. Y oung, F. Zheng, and A. M. Rappe, Prediction of a Linear Spin Bulk Photovoltaic Effect in Antiferromagnets, Phys. Rev. Lett. **110**, 057201 (2013).

[32] R. X. Fei, W. S. Song, L. P. Nazzaro, and L. Yang, *PT*-Symmetry-Enabled Spin Circular Photogalvanic Effect in Antiferromagnetic Insulators, Phys. Rev. Lett. **127**, 207402 (2021).

[33] X. X. Tao, P. Jiang, H. Hao, X. H. Zheng, L. Zhang, and Z. Zeng, Pure spin current generation via photogalvanic effect with spatial inversion symmetry, Phys. Rev. B **102**, 081402(R) (2020).

[34] F. Freimuth, S. Blügel, and Y. Mokrousov, Charge and spin photocurrents in the Rashba model, Phys. Rev. B **103**, 075428 (2021).

[35] Y. Q. Xie, M. Y. Chen, Z. W. Wu, Y. B. Hu, Y. Wang, J. Wang, and H. Guo, Two-Dimensional Photogalvanic Spin-Battery, Phys. Rev. Appl. **10**, 034005 (2018).

[36] Y. Li, J. Fu, X. Y. Mao, C. Chen, H. Liu, M. Gong, and H. L. Zeng, Enhanced bulk photovoltaic effect in two-dimensional ferroelectric $CuInP_2S_6$, Nat. Comm. **12**, 5896 (2021).

[37] D. S. Knoche, M. Steimecke, Y. Yun, L. Mühlenbein, and A. Bhatnagar, Anomalous circular bulk photovoltaic effect in $BiFeO_3$ thin films with stripe-domain pattern, Nat. Comm. **12**, 282 (2021).

[38] J. Zhao, Y. B. Hu, Y. Q. Xie, L. Zhang, and Y. Wang, Largely Enhanced Photogalvanic Effects in a Phosphorene Photodetector by Strain-Increased Device Asymmetry, Phys. Rev. Appl. **14**, 064003 (2020).

[39] T. Akamatsu, T. Ideue, L. Zhou, Y. Dong, S. Kitamura, M. Yoshii, D. Y. Yang, Ma. Onga, Y. Nakagawa, K. Watanabe, T. Taniguchi, J. Laurienzo, J. W. Huang, Z. L. Ye, T. Morimoto, H. T. Yuan, and Y. Iwasa, A van der Waals interface that creates in-plane polarization and a spontaneous photovoltaic effect, Science **372**, 68 (2021).

[40] L. E. Henrickson, Nonequilibrium photocurrent modeling in resonant tunneling photodetectors, J. Appl. Phys. **91**, 6273 (2002).

[41] L. Zhang, K. Gong, J. Z. Chen, L. Liu, Y. Zhu, D. Xiao, and H. Guo, Generation and transport of valley-polarized current in transition-metal dichalcogenides, Phys. Rev. B **90**, 195428 (2014).

[42] Y. Q. Xie, L. Zhang, Y. Zhu, L. Liu, and H. Guo, Photogalvanic effect in monolayer black phosphorus, Nanotechnology **26**, 455202 (2015).

[43] J. Taylor, H. Guo, and J. Wang, *Ab initio* modeling of quantum transport properties of molecular electronic devices, Phys. Rev. B **63**, 245407 (2001).

[44] For details of NANODCAL quantum transport package, see http://www.hzwtech.com.

[45] J. P. Perdew, K. Burke, and M. Ernzerhof, Generalized Gradient Approximation Made Simple, Phys. Rev. Lett. **78**, 3865 (1997).

[46] S. D. Ganichev, E. L. Ivchenko, H. Ketterl, W. Prettl, and L. E. Vorobjev, Circular photogalvanic effect induced by monopolar spin orientation in *p*-GaAs/AlGaAs multiple-quantum wells, Appl. Phys. Lett. **77**, 3146 (2000).

[47] S. D. Ganichev, E. L. Ivchenko, S. N. Danilov, J. Eroms, W. Wegscheider, D. Weiss, and W. Prettl, Conversion of Spin into Directed Electric Current in Quantum Wells, Phys. Rev. Lett. **86**, 4358 (2001).

[48] S. D. Ganichev, V. V. Bel'kov, P. Schneider, E. L. Ivchenko, S. A. Tarasenko, W. Wegscheider, D. Weiss, D. Schuh, E. V. Beregulin, and W. Prettl, Resonant inversion of the circular photogalvanic effect in *n*-doped quantum wells, Phys. Rev. B **68**, 035319 (2003).

[49] H. Ma, C. Y. Jiang, Y. Liu, J. L. Yu, and Y. H. Chen, Helicity dependent photocurrent enabled by unpolarized radiation in a $GaAs/Al_0.3Ga_0.7As$ two-dimensional electron system, Appl. Phys. Lett. **102**, 212103 (2013).

[50] Z. R. Ji, G. R. Liu, Z. Addison, W. J. Liu, P. Yu, H. Gao, Z. Liu, A. M. Rappe, C. L. Kane, E. J. Mele, and R. Agarwal, Spatially dispersive circular photogalvanic effect in a Weyl semimetal, Nat. Mater. **18**, 955 (2019).

[51] J. C. Ma, R. A. Muniz, S. M. Qi, J. W. Lai, K. N. Zhang, Y. N. Liu, X. Zhuo, S. X. Chen, J. H. Chen, S. Y. Zhou, and D. Sun, Circular photogalvanic effect from third-order nonlinear effect in 1T-$MoTe_2$, 2D Mater. **8**, 025016 (2021).

[52] Y. Pan, Q. Z. Wang, A. L. Yeats, T. Pillsbury, T. C. Flanagan, A. Richardella, H. Zhang, D. D. Awschalom, C. X. Liu, and N. Samarth, Helicity dependent photocurrent in electrically gated $(Bi_{1-x}Sb_x)_2Te_3$ thin films, Nat. Commun. **8**, 1037 (2017).

[53] Y. Z. Luo, Y. B. Hu, and Y. Q. Xie, Highly polarization-sensitive, visible-blind and self-powered ultraviolet photodetection based on two-dimensional wide bandgap semiconductors: A theoretical prediction, J. Mater. Chem. A **7**, 27503 (2019).

[54] N. Zuo, A. Nie, C. G. Hu, W. F. Shen, B. Jin, X. Z. Hu, Z. Y. Liu, X. Zhou, and T. Y. Zhai, Synergistic additive-assisted growth of 2D ternary In_2SnS_4 with giant gate-tunable polarization-sensitive photoresponse, Small **17**, 2008078 (2021).

[55] Y. S. Yang, S. C. Liu, X. Wang, Z. B. Li, Y. Zhang, G. M. Zhang, D. J. Xue, and J. S. Hu, Polarization-sensitive ultraviolet photodetection of anisotropic 2D GeS_2, Adv. Funct. Mater. 1900411 (2019).

[56] R. Huang, D. H. Lin, J. Y. Liu, C. Y. Wu, D. Wu, and L. B. Luo, Nanochannel-confined growth of crystallographically orientated perovskite nanowire arrays for polarization-sensitive photodetector application, Sci. China Mater. **64**, 2497 (2021).

[57] Y. Xin, X. X. Wang, Z. Chen, D. Weller, Y. Y. Wang, L. J. Shi, X. Ma, C. J. Ding, W. Li, S. Guo, and R. B. Liu, Polarization-sensitive self-powered type-II GeSe/MoS_2 van der Waals heterojunction photodetector, ACS Appl. Mater. Inter. **12**, 15406 (2020).

[58] J. Qiao, F. Feng, Z. M. Wang, M. Y. Shen, G. P. Zhang, X. C. Yuan, and M. G. Somekh, Highly in-plane anisotropic two-dimensional ternary Ta_2NiSe_5 for polarization-sensitive photodetectors, ACS Appl. Mater. Inter. **13**, 17948 (2021).

[59] Z. H. Ren, P. Wang, K. Zhang, W. H. Ran, J. H. Yang, Y. Y. Liu, Z. Lou, G. Z. Shen, and Z. M. Wei, Short-wave near-infrared polarization sensitive photodetector based on GaSb nanowire, IEEE Electr. Device L. **42**, 4 (2021).

[60] P. K. Venuthurumilli, P. D. Ye, and X. f. Xu, Plasmonic resonance enhanced polarization sensitive photodetection by black phosphorus in near infrared, ACS Nano **12**, 4861 (2018).

[61] J. X. Xiong, Y. M. Sun, L. G. Wu, W. Z. Wang, W. Gao, N. J. Huo, and J. B. Li, High performance self-driven polarization-sensitive photodetectors based on GeAs/InSe heterojunction, Adv. Optical Mater. 2101017 (2021).

[62] J. Bullock, M. Amani, J. Cho, Y. Z. Chen, G. H. Ahn, Va. Adinolfi, V. R. Shrestha, Y. Gao, K. B. Crozie, Y. L. Chueh, and A. Javey, Polarization-resolved black phosphorus/molybdenum disulfide mid-wave infrared photodiodes with high detectivity at room temperature, Nat. Photonics **12**, 601 (2018).

[63] D. Wu, J. W. Guo, J. Du, C. X. Xia, L. H. Zeng, Y. Z. Tian, Z. F. Shi, Y. T. Tian, X. J. Li, Y. H. Tsang, and J. S. Jie, Highly polarization-sensitive, broadband, self-powered photodetector based on graphene/$PdSe_2$/germanium heterojunction, ACS Nano **13**, 9907 (2019).

[64] S. D. Ganichev and W. Prettl, Spin photocurrents in quantum wells, J. Phys. Condens. Matter **15**, R935 (2003).

[65] A. A. Grinberg and S. Lury, Theory of the photon-drag effect in a two-dimensional electron gas, Phys. Rev. B **38**, 87 (1988).

[66] V. A. Shalygin, M. D. Moldavskaya, S. N. Danilov, I. I. Farbshtein, and L. E. Golub, Circular photon drag effect in bulk tellurium, Phys. Rev. B **93**, 045207 (2016).

[67] L. K. Shi, D. Zhang, K. Chang, and J. C. W. Song, Geometric Photon-Drag Effect and Nonlinear Shift Current in Centrosymmetric Crystals, Phys. Rev. Lett. **126**, 197402 (2021).

[68] V. I. Belinicher, E. L. Ivchenko, and B. I. Sturma, Kinetic theory of the displacement photovoltaic effect in piezoelectrics, Sov. Phys. JETP **56**, 359 (1982).

[69] J. Quereda, J. Hidding, T. S. Ghiasi, B. J. van Wees, C. H. van der Wal, and M. H. D. Guimaraes, The role of device asymmetries and Schottky barriers on the helicity-dependent photoresponse of 2D phototransistors, npj 2D Mater. Appl. **5**, 13 (2021).

[70] N. Meyer, K. Geishendorf, J. Walowski, A. Thomas, and M. Munzenberg, The impact of metallic contacts on spin-polarized photocurrents in topological insulator Bi_2Se_3 nanowires, Appl. Phys. Lett. **117**, 262401 (2020).

[71] M. Nakamura, H. Hatada, Y. Kaneko, N. Ogawa, Y. Tokura, and M. Kawasaki, Impact of electrodes on the extraction of shift current from a ferroelectric semiconductor SbSI, Appl. Phys. Lett. **113**, 232901 (2018).

[72] Y. Liu, P. Stradins, and S. H. Wei, Van der Waals metal-semiconductor junction weak Fermi level pinning enables effective tuning of Schottky barrier, Sci. Adv. **2**, e1600069 (2016).

Correction: The last term in Eq. (5) was missing and has been corrected.